A Ripple-Mitigating and Energy-Efficient Fuel Cell Power-Conditioning System

Sudip K. Mazumder, *Senior Member, IEEE*, Rajni K. Burra, *Member, IEEE*, and Kaustuva Acharya, *Student Member, IEEE*

***Abstract*—We describe an energy-efficient, fuel-cell power-conditioning system (PCS) for stationary application, which reduces the variations in the current drawn from the fuel-cell stack and can potentially meet the $40/kW cost target. The PCS consists of a zero-ripple boost converter (ZRBC) followed by a soft-switched and multilevel high-frequency (HF) inverter and a single-phase cycloconverter. The ZRBC comprises a new zero-ripple filter (ZRF), which significantly reduces the input low- and high-frequency current ripples, thereby potentially enhancing the durability of the stack. A new phase-shifted sinewave modulation of the multilevel HF inverter is proposed, which results in the zero-voltage switching (ZVS) of all four switches without the use of any auxiliary circuit components. For such a sine wave modulation technique, $>90\%$ ZVS range is obtained per line cycle for about 70% of the rated load. Further, the line-frequency switching of the cycloconverter (at close to unity power factor) results in extremely low switching losses. The intermediate dc bus facilitates the inclusion of power systems based on other forms of alternative-energy techniques (e.g., photovoltaic/high-voltage stack). A 5 kW prototype of the proposed PCS is built, which currently achieves a peak efficiency of 92.4%. We present a detailed description of the operation of the PCS along with its key features and advantages. Finally, experimental results showing the satisfactory performance and the operation of the PCS are demonstrated.**

***Index Terms*—Active power filter (APF), conditioner, cycloconverter, efficiency, fuel cell, grid, inverter, modulation, multilevel, photovoltaics, power-conditioning system (PCS), ripple reduction, zero ripple filter (ZRF).**

List of Abbreviations

PCS	Power-conditioning system.
ZRBC	Zero-ripple boost converter.
HF	High frequency.
LFSC	Line-frequency-switched cycloconverter.
SPWM	Sinewave pulse-width modulation.
ZRF	Zero-ripple filter.
APF	Active power filter.

Manuscript received November 29, 2005; revised May 30, 2006. This work was supported in part by the U.S. Department of Energy (DOE) and the California Energy Commission (CEC) under Awards DE-FG36-05GO15018 and EISG# 03-02k, in part by the DOE under Award DE-FC2602NT41574. The work of S. K. Mazumder was supported by a 2003 National Science Foundation CAREER Award 0239131. Recommended for publication by Associate Editor K. Ngo. This paper was presented in part at the 2004 IEEE International Telecommunications Energy Conference (INTELEC) and at the 2005 ASME Third International Conference on Fuel Cell Science, Engineering and Technology.

S. K. Mazumder is with the Laboratory for Energy and Switching-Electronics Systems, Department of Electrical and Computer Engineering, University of Illinois at Chicago, Chicago, IL 60607-7053 USA (e-mail: mazumder@ece.uic.edu).

R. K. Burra is with GE India Technology Centre Pvt. Ltd., Bangalore - 560 066, India.

K. Acharya is with the Department of Electrical and Computer Engineering, University of Illinois at Chicago, Chicago, IL 60607-7053 USA.

Color versions of one or more of the figures in this paper are available online at http://ieeexplore.ieee.org.

Digital Object Identifier 10.1109/TPEL.2007.900598

I. Introduction

IN ORDER TO maximize the efficiency of the fuel cell power system, the operating point of a fuel-cell stack should be chosen close to the maximum power-delivery point [as shown in Fig. 1(a)]. However, since the power-conditioning system (PCS) connected to the fuel-cell stack usually draws a current, which has a low-frequency ripple (e.g., 120 Hz for single- and split-phase systems) and a high-frequency (HF) switching ripple, the hydrogen utilization and fuel-cell efficiency varies over the nominal dc operating point of the stack. As a result, the operating point of the fuel cell is periodically forced into the concentration or the mass-transport region where the fuel-cell stack suffers from excessive losses and overheating [1], [2]. In order to avoid the periodic operation of the fuel cell in the concentration region, the dc operating point has to be reduced below the maximum power-delivery (and maximum-efficiency point), as shown in Fig. 1(a). However, such a reduction will result in a decrease in the efficiency of the fuel-cell stack, which is not desirable. In Fig. 1(b), the bar chart shows the maximum allowable hydrogen utilization for seven different values of fuel cell output-current ripple, from which the following conclusions can be drawn: (a) fuel-cell stack efficiency increases with increase in hydrogen utilization and (b) with increasing fuel cell current ripple, the maximum allowable hydrogen utilization decreases. Also, in [25], [31], it has been demonstrated that current ripple results in loss of fuel-cell stack power and has a degrading effect on its long-term performance.

Thus, to ensure energy-efficient operation of the fuel-cell stack, the output current ripple of the fuel-cell stack should be minimized. In [3], it is suggested that, that the magnitude of the low-frequency ($<$400 Hz) current ripple should be minimized to increase the durability of the fuel cell. In [4], an experimental impedance model of the proton exchange membrane fuel cell (PEMFC) has been demonstrated. It is shown that, the 120-Hz ripple current of the power conditioner can contribute to a reduction in the available output power of the fuel-cell stack and increased distortion of the terminal voltage. It is shown that, for PEMFC the size of the current ripple needs to be less than 30% for energy-efficient operation. In [5], a high power interleaved boost converter for fuel-cell systems is discussed,

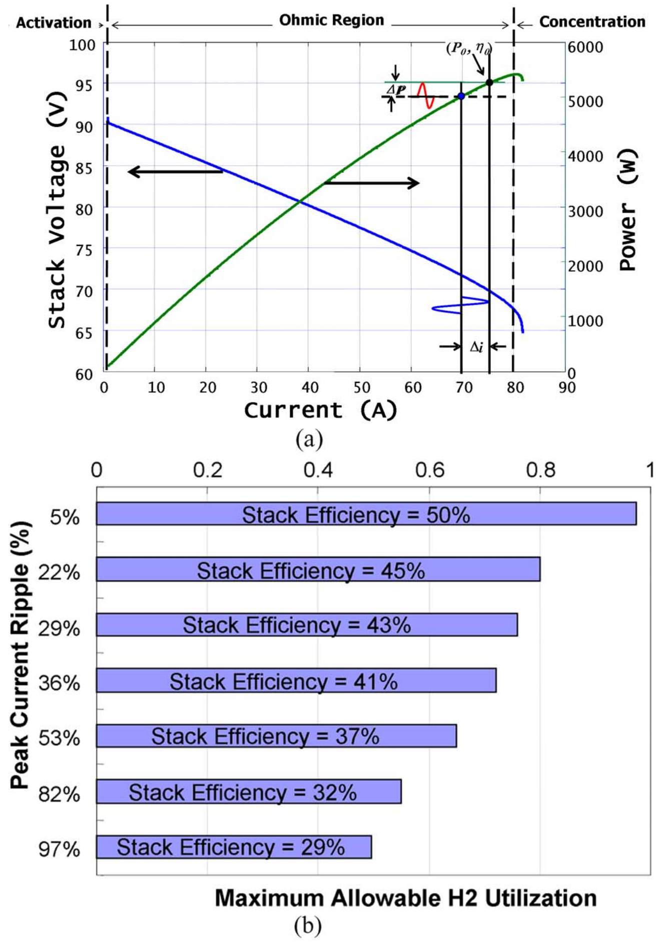

Fig. 1. Illustration of the fuel-cell characteristics: (a) simulated voltage–current and power–current characteristics plot for a 100-cell planar solid-oxide fuel-cell (SOFC). It shows the activation, ohmic (normal operating region), and concentration regions [29] of operation of the stack. The maximum power is obtained close to the rated current of the stack. (b) The maximum allowable hydrogen utilization and stack efficiency with variations in fuel-cell current ripple.

which can reduce the HF switching ripple. In [6], a new inverter current control is proposed, which achieves an active low-frequency current-ripple reduction. However, the proposed ripple-reduction method works effectively only in the presence of a bulky capacitor at the boost converter output. In [7], an active power filter (APF) for low-frequency ripple elimination is demonstrated, but it is not a part of fuel-cell power conditioner.

While improving the energy density of the fuel cell is necessary, it is also important to reduce the losses of the PCS to deliver the power of the fuel-cell stack efficiently to the load. The choice of power-electronic topologies can be broadly categorized as push-pull and full-bridge based topologies. In [8]–[11], low cost push-pull topology for power levels >1 kW is proposed. Push-pull based topology, owing to its low part count, is a good candidate for a low-cost fuel cell converter and can achieve an efficiency of 90% for low and medium power. However, at higher power it can suffer from transformer flux imbalance and core-saturation problems.

For current-fed topologies, the main limitation is encountered at greater than 3 kW, where, leakage inductance of the transformer poses a problem, unless soft switching is used. Further, the limited available range of switch duty cycle also makes it difficult to track variations in the input voltage.

In [12]–[18], full-bridge based fuel cell inverter topologies are discussed. Because of the symmetrical transformer flux and equal electrical-stress distribution, several variations of full-bridge inverter topologies have been found to be useful from the cost and efficiency point of view, especially when implemented for power levels greater than 3 kW. A 1.8 kW prototype of a boost converter followed by a two-stage dc–ac converter is discussed in [13]. The two-stage dc–ac converter comprising a full-bridge HF inverter and a cycloconverter, both operating at the same switching frequency, is based on a novel multicarrier pulse-width modulation (PWM) scheme. A similar two-stage dc–ac converter is discussed in [17], which incorporates a zero-current switched cycloconverter; while the full-bridge HF inverter is switched with a fixed 50% duty cycle. An improved version of the prototype in [17], comprising a soft-switched sinewave PWM (SPWM) full-bridge HF inverter followed by a cycloconverter (operating at line frequency) is proposed in [18]. Among all the low-cost fuel cell inverters [8]–[18], which aim to achieve an efficiency of greater than 90%, a maximum full-load efficiency of 87% and 89% is demonstrated in [8] and [18], respectively. *Also, the PCS topologies in [8]–[18] are not designed to improve efficiency of the stack.*

In [15], [23], a low-cost fuel-cell inverter for residential application has been presented. This converter also has a high-frequency link as in the cycloconverter topologies discussed above. However, instead of achieving a high-frequency dc–ac followed by an ac–ac forced cycloconversion, this topology first achieves a high-frequency isolated dc–dc conversion followed by dc–ac conversion using a full-bridge inverter. This topology has an *estimated* peak efficiency of 92% at 5 kW. *However, no measured efficiency results are provided. Further, it has no mechanisms to mitigate and reduce the high- and low-frequency current ripples.*

In a more recent [24], a voltage-clamped and soft-switching based fuel-cell inverter has been proposed, which has a measured peak efficiency of 95%. However, the peak power is only 350 W (which is $<$ 10% of the power requirement for residential fuel-cell inverters). Further, the inverter apparently does not have any high-frequency transformer for galvanic isolation (which is necessary). The presence of the transformer reduces the overall efficiency. On the other hand, if [24] uses line-transformer for isolation, then the weight and size of the converter will be significant. *Finally, this converter also does not have any ripple-mitigating mechanism in the topology.*

In this paper, we present a low-cost and energy-efficient PCS [Fig. 2(a)], which significantly reduces the fuel-cell ripple current. The mechanism of ripple mitigation is based on a *zero-ripple filter (ZRF)* that comprises a coupled inductor based filter [27] for minimizing the high-frequency switching ripple and an APF for mitigating the low-frequency ripple. We believe this is the *first paper* on fuel-cell inverter that provides a topological mechanism [see Fig. 2(a)] that mitigates both low- and high-frequency ripples of the stack current. As illustrated in Fig. 1, by reducing the current ripple, one can enable the fuel-cell stack to operate closer to its maximum-efficiency point. Thus, the

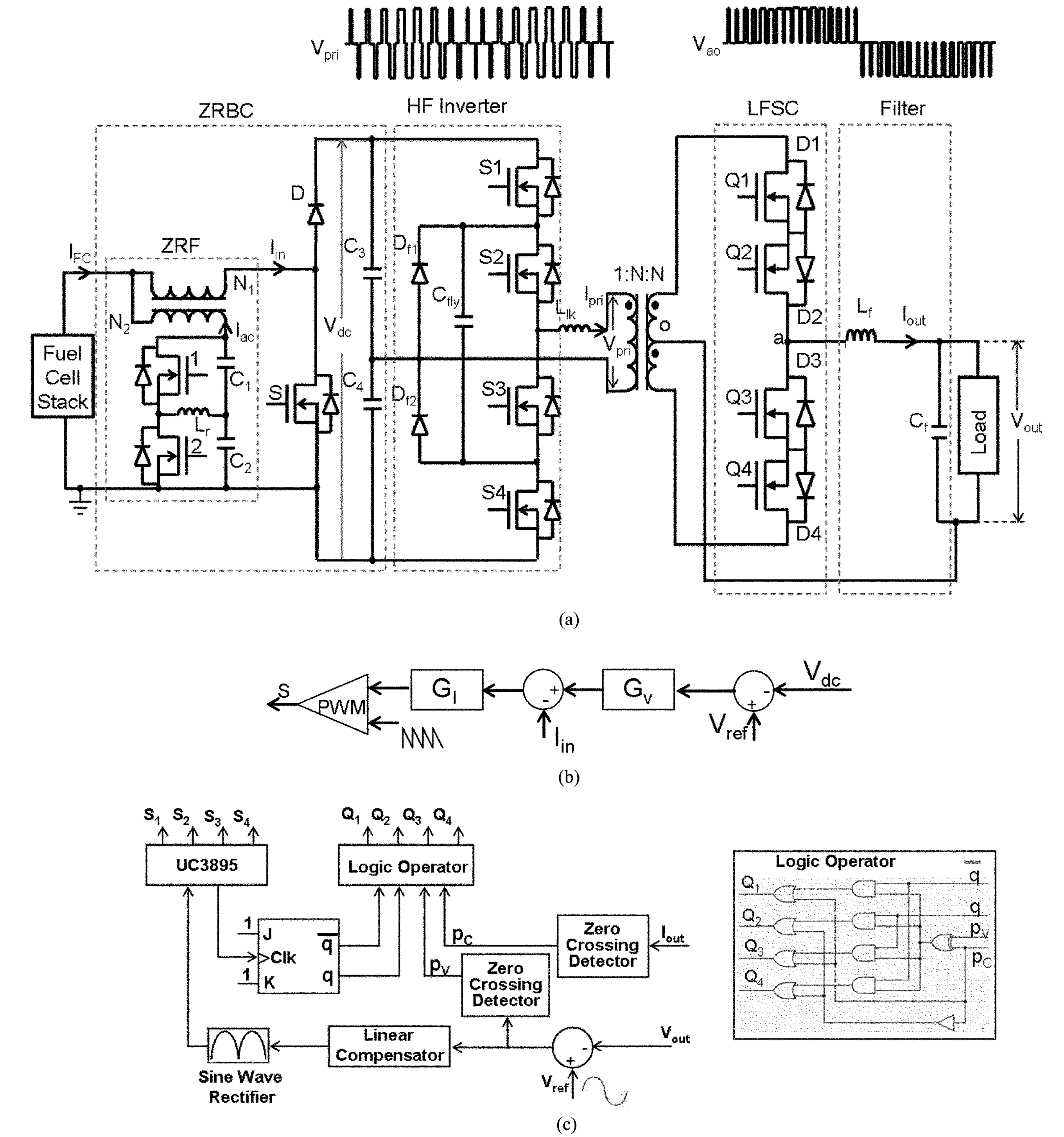

Fig. 2. (a) Schematic of the proposed PCS, which comprises a ZRBC connected to the fuel-cell stack and it is followed by an isolated dc–ac converter comprising the HF inverter, HF transformer (with $N = N_s/N_p$and the LFAC. Although, only one ZRBC module is shown, for actual experiments, four such modules are connected in parallel to reduce the conduction loss by sharing the large stack current. (b) Current-mode control scheme for the ZRBC. (c) Control scheme for the overall dc–ac converter.

overall energy efficiency of the fuel-cell power system (which is a product of the efficiencies of the fuel-cell stack and the power electronics) will increase considerably. The overall efficiency of the total energy system is of higher importance to the end user than the efficiency of the power electronics alone.

Reducing the ripple of the fuel-cell current not only has an impact on the stack efficiency but also on its performance and durability. For instance, in [25] it has been demonstrated (using 1000 hours of test) that if two similar planar solid-oxide fuel cell (SOFC) stacks are subjected to only a dc current and the same dc current with additional current ripple, respectively, then, for the second scenario, the area-specific resistance of the stack may increase at a higher rate. The latter translates to progressive loss of stack power and degradation.

Finally, *reducing the current ripple using the ZRF based PCS also enables better utilization of the fuel-cell stack.* As shown [Fig. 1(a)] in the voltage–current (V–I) characteristics of a planar a SOFC, if the stack is subjected only to a dc current, then, its output voltage reduces only when the stack output current increases in magnitude. However, if the stack output current has a ripple component on top of a dc current, then the stack output voltage will swing even for the same dc current. Consequently, to meet the efficiency requirement of the follow-up converter in the presence of varying stack voltage, one may be forced to limit the load current or for the same load current use a stack with higher current capability. This will be a costly proposition because the cost of a stack is usually lot higher than that of power electronics.

Apart from the ZRF, which is integrated with a boost converter to yield a zero-ripple boost converter (ZRBC), the PCS in Fig. 2(a) comprises a followup low-loss isolated dc–ac converter. The first stage of this dc–ac converter comprises a soft-switched phase-shifted sinewave PWM (SPWM) multilevel zero-voltage-switching (ZVS) HF inverter, which is followed by a line-frequency-switched cycloconverter (LFSC) [18]. We believe this is the *first time*, a topology comprising multilevel HF inverter followed by an LFSC has been demonstrated for fuel-cell-inverter application. In [21], [26], a three-level inverter is designed. However, its application is for dc–dc application (instead of dc–ac application). As such, the secondary of this isolated dc–dc converter comprises an ac–dc rectifier and not a cycloconverter. These differences have an impact on the parametric design and efficiency of the PCS, which are addressed in this paper. For instance, for dc–ac applications, not only the load but also line variations are important which have an impact on the commutation losses and efficiency of the system. The multilevel arrangement of the HF inverter switches reduces the voltage stress and the cost of the semiconductor switches. This will be of interest when using the inverter for high-power and high-voltage applications. The LFSC is switched at ac line frequency based on the power-flow information leading to considerably low switching losses. Therefore, the heat-sinking requirements of the LFSC switches are significantly reduced.

Section II of this paper discusses the overall PCS schematic. It provides a detailed description on the following: i) a discussion on the ZRBC comprising the ZRF and the mechanisms for high- and low-frequency current-ripple mitigations; ii) discussions on the isolated dc–ac converter with regard to modes of operation, ZVS range of the HF inverter, and leakage optimization of the high-frequency isolation transformer for energy-efficient design. Section III provides hardware setup, values of key parameters of the PCS, detailed experimental results showing performances of the ZRBC and dc–ac converter under steady-state and transient conditions and the overall energy-conversion efficiency of the PCS (as well as ZRBC and the dc–ac converter). Section IV draws conclusions from the results and the design tradeoffs while Section V illustrates the application of the presented PCS for other energy sources.

II. Description of the PCS

The PCS [shown in Fig. 2(a)] consists of a dc–dc converter, which steps up the input dc voltage of the fuel-cell stack, and is followed by a dc–ac inverter, the output of which can be fed to a standalone load or a utility grid. The energy buffering for the fuel-cell PCS can be provided by standard add-on battery-based power conditioner (connected across capacitors C3 and C4) or by direct grid support [30]. The 5 kW 20 kHz PCS unit, shown in Fig. 2(a), comprises a fuel-cell powered dc–dc ZRBC, which generates a high-voltage dc at its output.. The ZRBC is followed by a soft-switched, transformer isolated dc–ac inverter, which generates a 110 V RMS ac. The HF inverter switches are arranged in a multilevel fashion and are modulated at 20 kHz by a fully-rectified sine wave to create a HF and three-level ac voltage V_{pri}, as shown in Fig. 2(a). The HF inverter is followed by the LFSC, which [as shown in Fig. 2(a)] basically rectifies this HF PWM waveform to generate a pulsating 40 kHz waveform that is almost similar to that of the output of a conventional voltage-source inverter (VSI) [20]. (We remind the readers that although the LFSC output is a 40 kHz waveform, its controlled power devices are still switching at line frequency.) The primary difference between the dc–ac converter in Fig. 2(a) and a VSI is that when the signal is rectified (i.e., the output signal of the LFSC), although the effective frequency doubles (40 kHz), the fundamental modulation of the pulses is still based at 20 kHz. In contrast, in a VSI, a 40 kHz output will require an actual 40 kHz switching of the power devices, which has implications on switching losses. However, frequency spectrums of the output of a 40 kHz VSI and the dc–ac converter [in Fig. 2(b)], with the HF inverter operating at 20 kHz and the ac–ac converter operating at line-frequency to rectify the inverter output, are slightly different. The output of the dc–ac converter is passed through a low-pass filter, which converts the three-level ac voltage to a sinusoidal output voltage with a line frequency of 60 Hz.

A. Zero-Ripple Boost Converter (ZRBC)

The ZRBC is a standard non-isolated boost converter, in which the conventional inductor is replaced with a ZRF. The ZRF [as shown in Fig. 3(c)] is viewed as a combination of a coupled inductor [shown in Fig. 3(a)] and a half-bridge active-power filter (APF) [shown in Fig. 3(b). The simple control mechanism for the master module is shown in Fig. 2(b). The outer voltage loop regulates V_{dc} using a linear compensator G_{v} and the current reference of the outer loop is compared with I_{in} for better dynamic response. Output of the current loop compensator (G_{I}) is compared with a ramp carrier to generate the PWM signal for switch S. Although we describe only one ZRBC below, in the actual implementation, four ZRBC modules were connected in parallel to reduce the conduction loss due to high source current (because a fuel-cell stack usually provides power at low voltage and high current). The PWM signals for the switches of all the other three modules are the same as that for switch S.

The hybrid structure of the ZRF serves the dual purpose of reducing the high- and the low-frequency current ripples so that I_{FC} (which is the current supplied by the fuel cell) is a dc. As shown in Fig. 3(a), the coupled inductor, in combination with capacitor C [in Fig. 3(a)] or equivalently identical capacitors C_1 and C_2 [in Fig. 3(c)], minimizes the HF ripple of the fuel-cell current (i.e., $i_{2\mathrm{HF}}$). On the other hand, the APF [shown in Fig. 3(b)] minimizes the low-frequency ripple of the fuel-cell

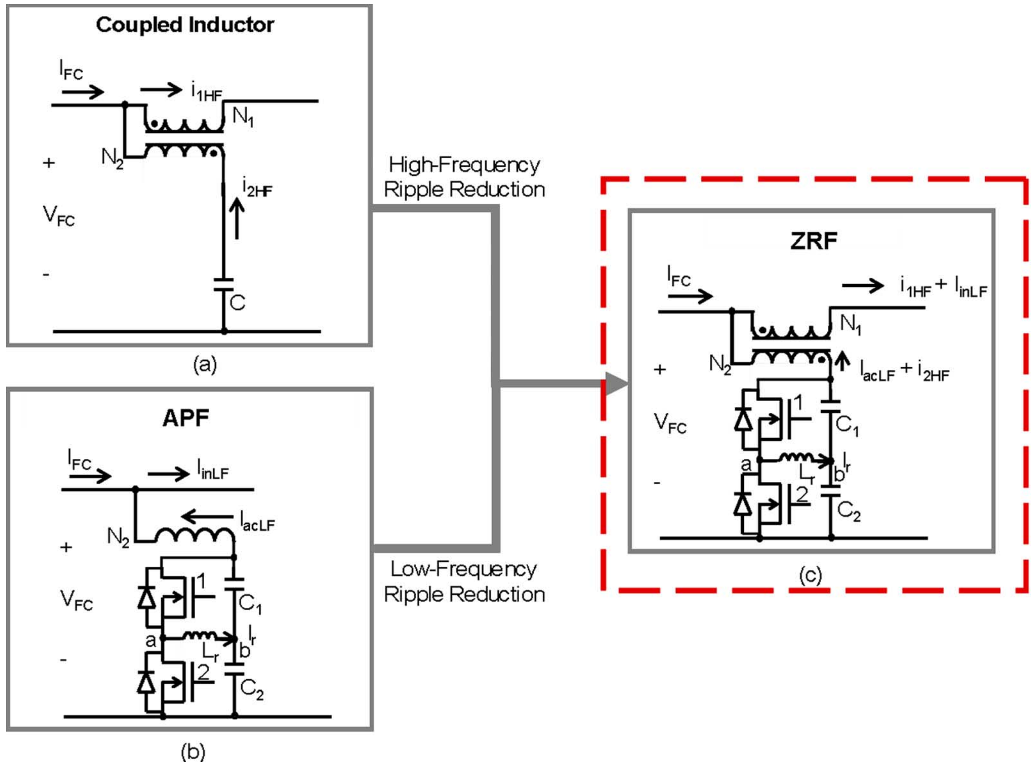

Fig. 3. Schematic diagrams for (a) coupled-inductor structure which reduces the HF current ripple [27]; (b) the half-bridge active filter which reduces low frequency ripple current of the fuel-cell stack; and (c) the schematic of the ZRF. For (c), with reference to Fig. 2(a), $I_{ac} = I_{acLF} + i_{2HF}$ and $I_{in} = I_{FC} + I_{ac}$.

current (i.e., I_{acLF}) by providing a low-impedance path via either storage reactor (L_r) and C_1 or L_r and C_2. Thus, in Fig. 3(c), for effective mitigation of the HF current from the fuel-cell output, the values of C_1 and C_2 should be so chosen such that the impedance of the path (formed by C_1 and C_2 and the coupled inductor) as seen by the high-frequency ripple current is much smaller than that seen by the low-frequency ripple current. Similarly, L_r should be so chosen such that the impedance of the path (formed by one of C_1 or C_2 and L_r) as seen by the low-frequency ripple current is much smaller than that seen by the high-frequency ripple current. Therefore, for a chosen value of capacitor (C), the following relations should hold true:

$$C_1 = C_2 = 2C \tag{1a}$$

$$f_{HF} = \frac{1}{2\pi\sqrt{L_{22}C}} \tag{1b}$$

$$f_{LF} = \frac{1}{2\pi\sqrt{2L_rC}} \tag{1c}$$

where L_{22} is the self inductance of the secondary winding of the coupled inductor (with N_2 turns) and f_{HF} and f_{LF} are the resonant frequencies. In the design of the APF, the value of L_r should be minimized. Therefore, assuming that

$$f_{HF} > 20f_{LF} \tag{1d}$$

the value L_{22} and L_r can be determined using

$$\frac{1}{\sqrt{L_{22}C}} > \frac{10\sqrt{2}}{\sqrt{L_rC}} \quad \text{or} \quad L_r > 200L_{22}. \tag{1e}$$

Therefore, the value of L_{22} should be small in order to limit the value of L_r and also to minimize the phase shift in low-frequency ripple current. Also, from a control standpoint, the values of L_{22}, L_r, and C should be chosen in such a way so that f_{HF} and f_{LF} and the ZRBC corner frequencies do not overlap and are separated by a decade.

1) HF Current-Ripple Reduction: In this section, the effective inductance offered by the coupled inductor and the achievable ripple reduction is derived. Because, the values of the capacitors C_1 and C_2 are large and that of L_{22} is small, the dynamics of the APF is assumed to have minimal effect on the coupled-inductor analysis. For the π-model of the coupled inductor, the excitation voltage and the current for the primary and the secondary windings are shown in the Fig. 4. The parameters of the coupled inductor are defined as follows:

$$k = \frac{M}{\sqrt{L_{22}L_{11}}} \tag{2a}$$

$$L_M = \frac{M}{n} \tag{2b}$$

$$n = \frac{N_2}{N_1} \cong \sqrt{\frac{L_{22}}{L_{11}}} \quad \text{(for low leakage)} \tag{2c}$$

$$L_{11} = L_1 + L_M \tag{2d}$$

where L_{11} is the primary side leakage inductance, and L_{11} and L_{22} are the self inductances of the primary and secondary windings, respectively, L_M is the primary magnetizing inductance, M is the mutual inductance, and k is the coupling coefficient of the coupled inductor. The currents i_{1HF} and i_{2HF} are the primary and the secondary ac currents, respectively, as shown in Fig. 4 and are derived using

$$v_{FC} = (L_1 + L_M)\frac{di_{1HF}}{dt} + nL_M\frac{di_{2HF}}{dt}. \tag{3a}$$

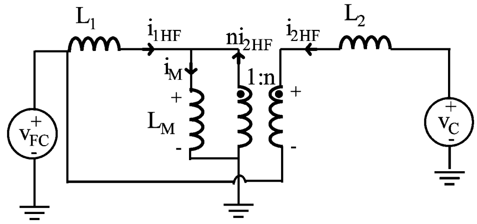

Fig. 4. AC π-model for the coupled inductor shown in Fig. 3(a).

$$\mathrm{v_C} = (\mathrm{L_1} + \mathrm{L_M} + \mathrm{nL_M})\frac{\mathrm{di_{1HF}}}{\mathrm{dt}} + (\mathrm{L_2} + \mathrm{nL_M} + \mathrm{n^2L_M})\frac{\mathrm{di_{2HF}}}{\mathrm{dt}}. \tag{3b}$$

where $\mathrm{L_2}$ is the secondary side leakage inductance. To reduce the ac component of the fuel-cell-stack current to zero, the following condition should hold true:

$$\frac{\mathrm{di_{1HF}}}{\mathrm{dt}} = \frac{\mathrm{di_{2HF}}}{\mathrm{dt}}. \tag{4}$$

Using (2)–(4) and assuming negligible leakage, we obtain

$$\begin{aligned}\frac{\mathrm{di_{1HF}}}{\mathrm{dt}} &= \frac{\mathrm{v_{FC}}}{\mathrm{L_{11}}\left[1 + \frac{\mathrm{nL_M}}{\mathrm{L_{11}}}\right]} \\ &= \frac{\mathrm{v_{FC}}}{\mathrm{L_{11}}\left[1 + \frac{\mathrm{k}\sqrt{\mathrm{L_{22}L_{11}}}}{\mathrm{L_{11}}}\right]} \\ &= \frac{\mathrm{v_{FC}}}{\mathrm{L_{11}}\,(1 + \mathrm{kn})} \\ &= \frac{\mathrm{v_{FC}}}{\mathrm{L_{eff}}}.\end{aligned} \tag{5}$$

The denominator of (5) is the effective inductance $\mathrm{L_{eff}}$ exhibited by the coupled inductor of the ZRF.

Fig. 5(a) shows the dependence of the scaled $\mathrm{L_{eff}}$ on n as k is varied. For the values of the scaled $\mathrm{L_{eff}}$ shown in Fig. 5(a), the corresponding values of the achievable ripple current in both the coupled-inductor windings are shown in Fig. 5(b). Using Fig. 5(b), a designer can decide on a value of high-frequency current ripple and using the corresponding values of n and k, the scaled $\mathrm{L_{eff}}$ can be chosen using Fig. 5(a). However, while deciding on the value of k and n, the bandwidth requirements of the ZRBC must be kept in mind. An increase in $\mathrm{L_{eff}}$ has a two-pronged effect on the open-loop frequency response of the ZRBC. Firstly, the bandwidth is reduced and secondly, the right-half-plane zero is drawn closer to the imaginary axis, resulting in a reduction in the available phase margin.

2) Low-Frequency Ripple Reduction: We derive the condition for low-frequency current ripple elimination from the PCS input current (the low- and high-frequency dynamics of the ZRF are assumed practically independent of each other for a small secondary self inductance $\mathrm{L_{22}}$). For the APF shown in Fig. 3(b), the voltage across $\mathrm{L_r}$ is obtained as

$$\mathrm{V_{ab}} = \mathrm{V_a} - \frac{\mathrm{V_{FC}}}{2} = \mathrm{V_{FC}}\left(\mathrm{S_a} - \frac{1}{2}\right) \tag{6}$$

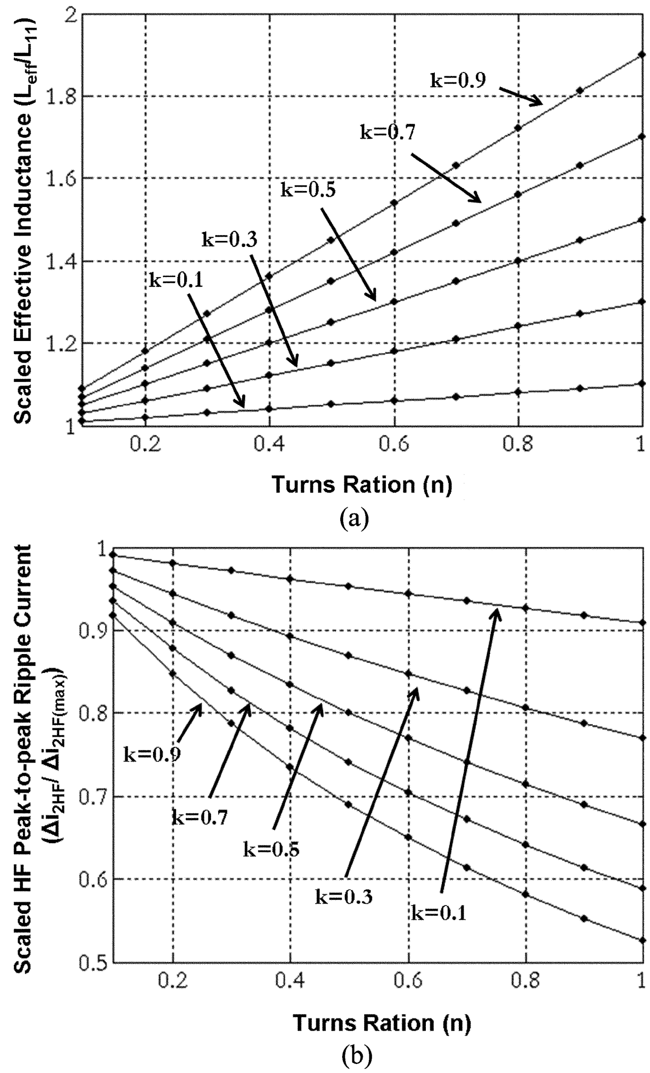

Fig. 5. (a) Scaled effective inductance and (b) scaled high-frequency peak-to-peak ripple current of the coupled inductor.

where $\mathrm{S_a}$ is given by

$$\mathrm{S_a} = 0.5 + \sum_{\mathrm{n}=1}^{\infty} \mathrm{B_n} \sin \mathrm{n}(\omega \mathrm{t} + \phi).$$

The current through $\mathrm{L_r}$ is given by

$$\mathrm{I_r} = \frac{\mathrm{V_{ab}}}{\mathrm{j}\omega\mathrm{L_r}} = \frac{\mathrm{V_{FC}}\left(\mathrm{S_a} - \frac{1}{2}\right)}{\mathrm{j}\omega\mathrm{L_r}}. \tag{7a}$$

Considering only the fundamental component of $\mathrm{I_r}$ in (7a), we obtain

$$\mathrm{I_r} = \frac{\mathrm{V_{FC}}}{\omega\mathrm{L_r}}\mathrm{B_1}\sin\left(\omega\mathrm{t} + \phi - \frac{\pi}{2}\right) \tag{7b}$$

using which the fundamental current injected by the APF is obtained as follows:

$$\begin{aligned}\mathrm{I_{acLF}} &= \left(\mathrm{S_a} - \frac{1}{2}\right)\mathrm{I_r} \\ &= \frac{\mathrm{V_{FC}}}{\omega\mathrm{L_r}}\mathrm{B_1^2}\sin(\omega\mathrm{t} + \phi)\sin\left(\omega\mathrm{t} + \phi - \frac{\pi}{2}\right) = -\frac{\mathrm{V_{FC}}}{2\omega\mathrm{L_r}} \\ &\quad \times \mathrm{B_1^2}\cos\left(2\omega\mathrm{t} + 2\phi - \frac{\pi}{2}\right).\end{aligned} \tag{8}$$

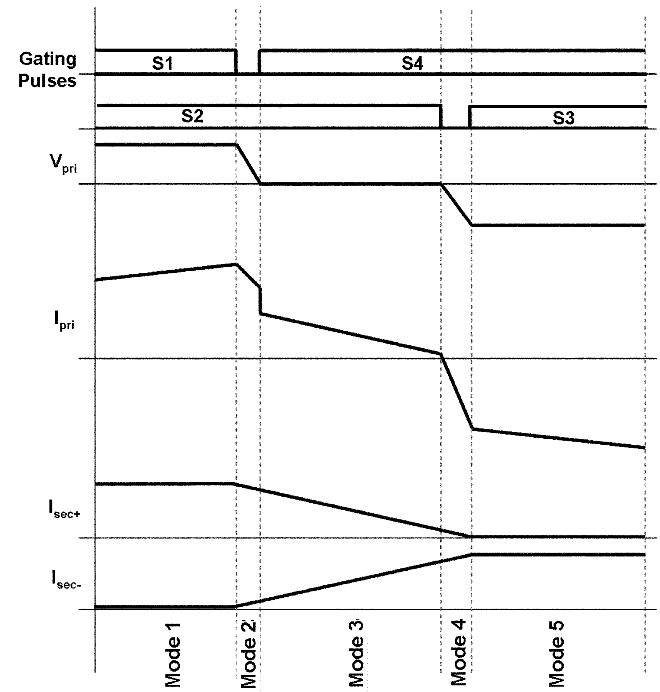

Fig. 6. Gating sequence of the HF inverter switches and illustration of its modes of operation.

Now, the input current of the PCS without the ZRF (but using a conventional boost inductor) comprises a dc component and a 120 Hz ac component and is expressed as

$$\mathrm{I_{FC}} + \mathrm{I_{ac}(t)} = \frac{\mathrm{V_{out,peak}I_{out,peak}}}{\eta \mathrm{V_{FC}}}\cos\theta - \frac{\mathrm{V_{out,peak}I_{out,peak}}}{\eta \mathrm{V_{FC}}}\cos(2\omega \mathrm{t} - \theta) \quad (9)$$

where I_{FC} is the dc component of the fuel cell output current; I_{ac} is the ac component of the fuel cell output current; $V_{out,peak}$ is the PCS peak output voltage; $I_{out,peak}$ is the inverter peak output current; V_{FC} is the fuel cell stack voltage; θ is the load power-factor angle; η is the energy efficiency of the PCS.

In order to reduce the 2nd harmonic component of the stack output current to zero, one needs to satisfy the condition $I_{acLF} = I_{ac}$, where I_{ac} is the ac component of the dc–ac inverter input current. Using this constraint and (8) and (9), we obtain the following:

$$\frac{\mathrm{V_{FC}}}{2\omega \mathrm{L_r}}\mathrm{B}_1^2\left[\cos\left(2\omega \mathrm{t} + 2\phi - \frac{\pi}{2}\right)\right] = \frac{\mathrm{V_{out,peak}I_{out,peak}}}{\eta \mathrm{V_{FC}}}\cos(2\omega \mathrm{t} - \theta) \quad \text{(10a)}$$

which yields

$$\mathrm{B}_1 = \frac{\sqrt{2\omega \mathrm{L_r V_{out,peak} I_{out,peak}}/\eta}}{\mathrm{V_{FC}}} \quad \text{(10b)}$$

provided

$$\phi = \frac{\pi}{4} - \frac{\theta}{2}. \quad \text{(10c)}$$

Therefore, in order to eliminate the 120 Hz from the fuel-cell output current, the modulating signal of the APF should have amplitude of B_1 and should be phase shifted by an angle of ϕ with respect to the modulating signal of the HF inverter.

B. DC–AC Converter

In this section, the ZVS operation of the dc–ac converter is discussed. A tradeoff analysis between the achievable ZVS range and duty ratio loss is done towards the end of this section. Such a study is necessary for energy-efficient design of the transformer-isolated topology. The control scheme for the dc–ac converter is described in Fig. 2(c). The switching pulses for the HF inverter are obtained by feeding the output of a voltage-loop controller (that regulates V_{out}) to UC3895. The latter creates phase-shifted ZVS SPWM pulses (shown in Fig. 6) for switches S1-S4. Fig. 6 shows the schematic waveforms of the five operating modes of the HF inverter for a positive primary current. Modes 2 and 4 show the ZVS turn-on mechanism for switches S4 and S3, respectively.

The LFSC modulation scheme [18], as illustrated in Fig. 2(c), is simple as well and its control relies on the signals V_{out} and I_{out}, which are sensed (without appreciable feedback delay) using Hall sensors. Basically, if the polarities of V_{out} and I_{out}, detected using two zero-crossing detectors are the same, then, either Q1 and Q4 or Q2 and Q3 are turned ON permanently for half a line cycle depending on whether V_{out} is positive or negative, respectively. The switches are, however, commutated at high frequency when the polarities of the output current and voltage are different. For near-unity power factor operation, this duration is small and therefore, the switching loss of the LFSC is considerably reduced compared to the conventional forced-switching control method [17].

1) Modes of Operation: In this section, five modes of the dc–ac converter operation are discussed for positive primary current. Additional five modes, that can be derived using the same procedure below, exist for a negative primary current.

Mode 1 [Fig. 7(a)]: During this mode, switches S1 and S2 of the HF inverter are turned ON and the transformer primary current I_{pri} is positive. The output current I_{out} is positive and flows through the bidirectional switch pair Q1 and Q2, the output filter, and the center-tap of the transformer secondary. Switches S3 and S4 and Q3 and Q4 are turned OFF during this interval.

Mode 2 [Fig. 7(b)]: At the beginning of this interval, the control signal of the switch S1 undergoes a high-to-low transition. As a result, the switch S1 begins to turn OFF. During this time, the output capacitance of S1 begins to charge, while the output capacitance of switch S4 begins to discharge through the fly capacitor (C_{fly}). During this time, the voltage across the primary of the transformer begins to fall towards zero. As a result the transformer primary current, I_{pri} also reduces. This mode of operation ends when the output capacitor of S4 has discharged completely and its output capacitance is charged to $V_{dc}/2$.

Mode 3 [Fig. 7(c)]: This mode initiated after the switch S1 is completely turned OFF, while the output capacitor of switch S4 is completely discharged. During this time, the switch S4 is turned ON under ZVS conditions. Because the voltage across

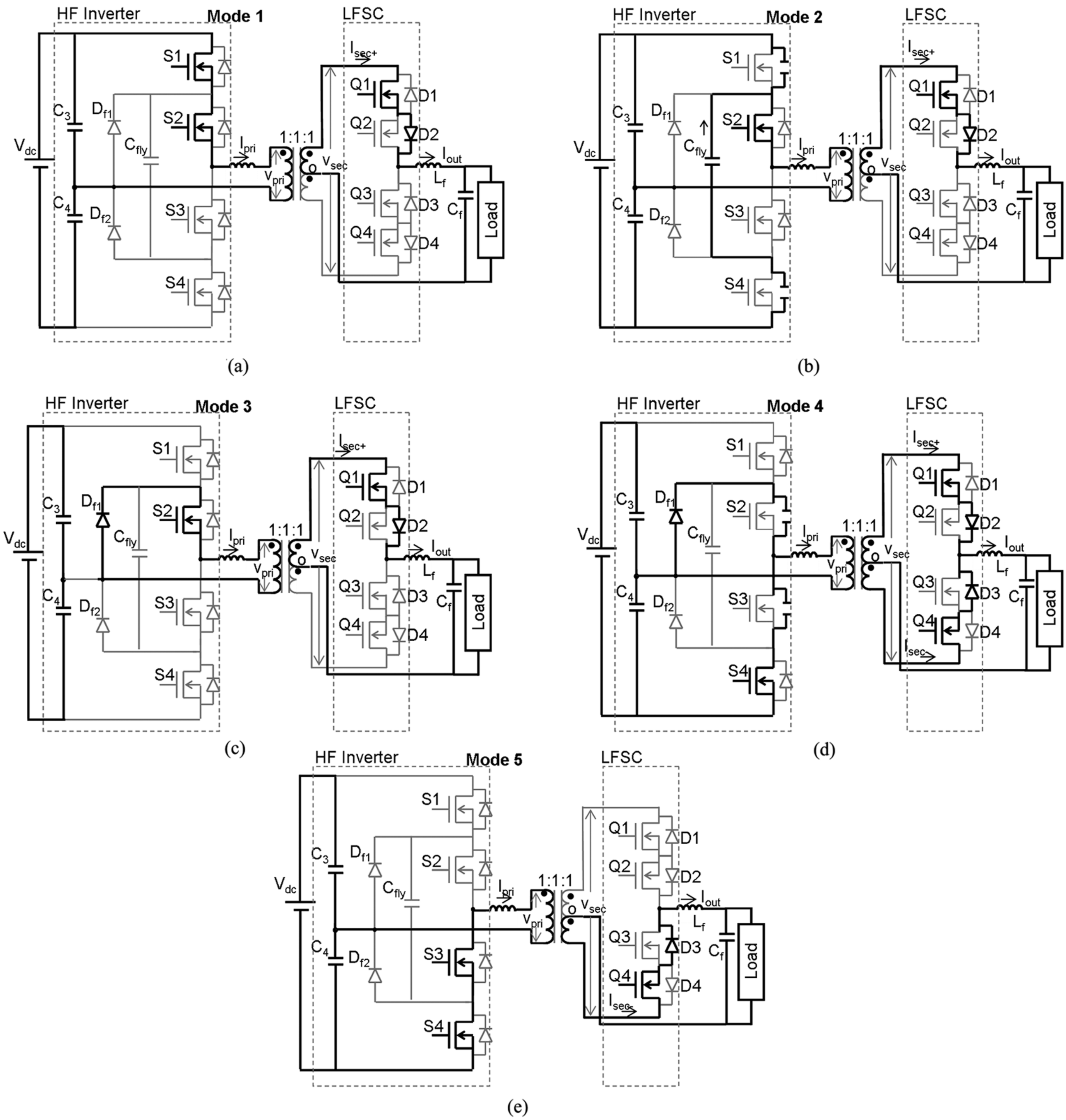

Fig. 7. Topologies corresponding to the five operating modes of the dc–ac converter for positive primary current and for power flow from the source to the load.

the primary of the transformer is zero, there is a sharp fall in the transformer primary current I_{pri} at the beginning of this mode. During this mode, the transformer primary current I_{pri} freewheels through the diode D1 as shown in Fig. 7(c) and continues to reduce in magnitude. The rate of decrease of the current is governed by the combined effects of the magnetizing inductance of the transformer and the output filter inductor.

Mode 4 [Fig. 7(d)]: At the beginning of this mode, the control signal of the switch S2 undergoes a high-to-low transition. As a result, the output capacitance of S2 begins to charge and at the same time, the output capacitance of switch S3 begins to discharge, as shown in the Fig. 7(d). The transformer current makes a transition from positive to negative. During this time, the flow of current on the secondary side makes a rapid transition from the bidirectional switches Q1 and Q2 to Q3 and Q4.

Mode 5 [Fig. 7(e)]: This mode starts when S2 is completely turned OFF and the voltage across its output capacitance is $V_{dc}/2$. Also, the output capacitance of switch S3 is completely

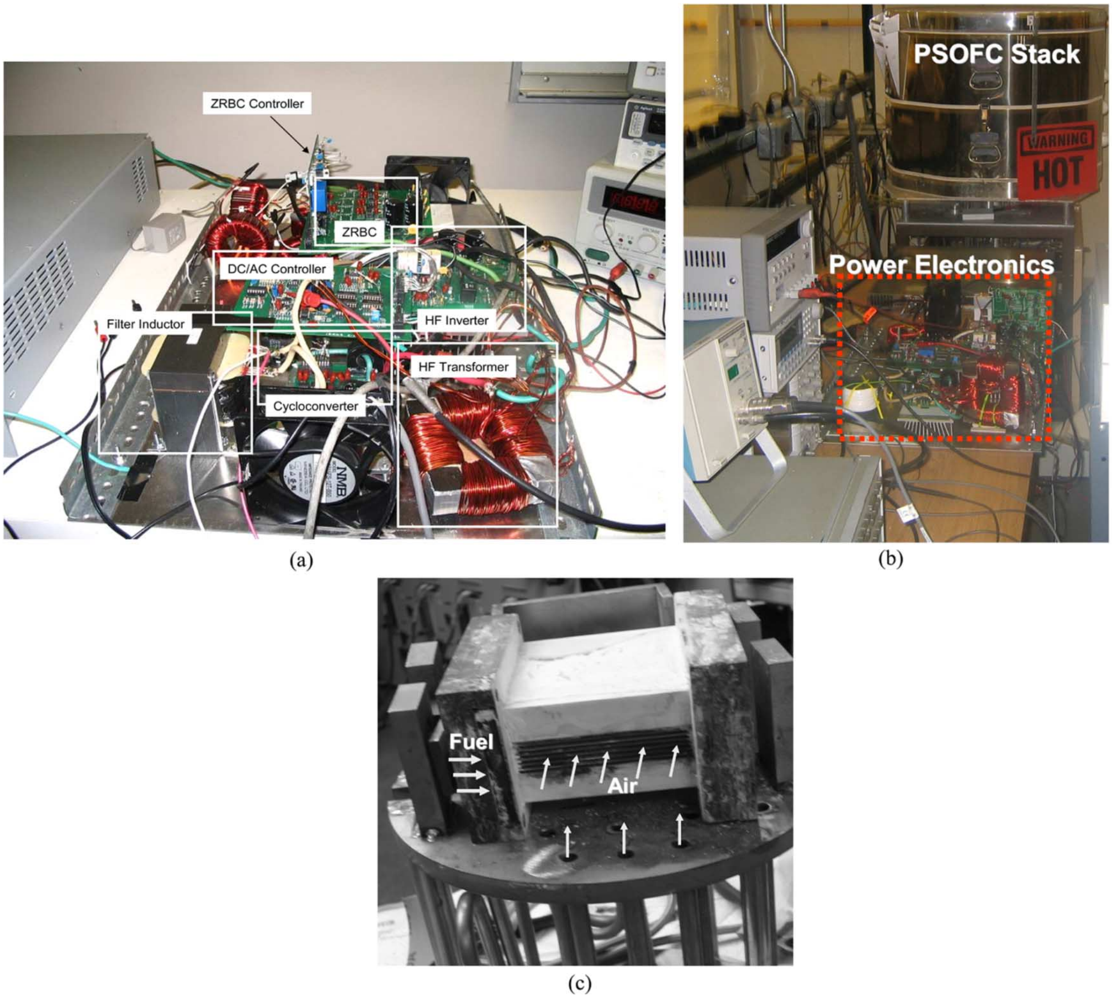

Fig. 8. (a) Experimental prototype of the proposed PCS. (b) Experimental setup for scaled testing with planar SOFC stack shown in (c).

discharged; as a result, the switch S3 can be turned ON under ZVS. During this mode, the transformer secondary current flows through switches Q3 and Q4, while the primary current increases in the opposite direction due to the negative voltage across the primary of the transformer.

2) ZVS Range of the HF Inverter: For the HF inverter, the SPWM results in ZVS loss for each switch, twice in every line cycle. The extent of ZVS loss is a function of the output current I_{out} (11) and the load power factor $\cos(\theta)$. Equation (12) is the expression of the available ZVS range as a percentage of the line cycle:

$$I_{out,peak} = \frac{2P_{in}\eta}{V_{out,peak}\cos(\theta)} \tag{11}$$

$$\frac{t_{ZVS}}{t_{LineCycle}} = \frac{2}{\pi}\sin^{-1}\left(\left(\frac{1}{2}\frac{V_{dc}^2\left(\frac{4}{3}C_{oss}+\frac{1}{2}C_T\right)}{I_{out,peak}^2 L_{lk}}\right)^{1/2}\right) \tag{12}$$

where P_{in} is the input power; V_{dc} is the input voltage to the dc–ac converter; L_{lk} is the leakage inductance of the primary transformer; C_T is the equivalent parasitic capacitance of the HF transformer; C_{oss} is the effective output capacitance of the MOSFETs of the HF inverter; $t_{LineCycle}$ is the line-cycle time period (for a 60 Hz line frequency it is 16.67 ms).

3) Leakage Optimization for Energy-Efficient Design: The effective duty ratio for the HF inverter is expressed in [21] as

$$D_{eff} = \frac{V_{out}}{V_{dc}} = \frac{2t_{on}}{T_s} - \frac{2}{T_s}\frac{2L_{lk}NI_{out}}{V_{dc}} + \frac{2}{T_s}\frac{V_{dc}C_{oss}}{2NI_{out}} \tag{13}$$

where t_{on} is time during which a non-zero voltage is applied across the transformer primary and T_s is the switching time period.

Equation (13) shows that as the leakage inductance of the HF transformer increases, D_{eff} reduces. Therefore, to maintain the output voltage for a given V_{FC}, the closed-loop controller has to increase the value of the first term in (13) by increasing t_{on}, which results in higher conduction losses for the HF inverter as well as for the LFSC. In contrast, (12) shows that for a given output current, a larger leakage inductance improves the ZVS range of the HF inverter switches, thereby reducing the switching losses. Therefore, design of the HF transformer and its winding arrangement play a key role in the energy-efficient design of the isolated dc–ac converter.

TABLE I
LIST OF THE KEY POWER-STAGE COMPONENTS FOR THE EXPERIMENTAL PCS

Designator	**Manufacturer**	**Part Number**	**Description**
S, Q1-Q4	IXYS	IXFX55N50	500 V, 55 A, 80 mΩ
S1-S4	IXYS	IXFX120N20	200 V, 120 A, 17 mΩ
D	Infineon Technologies	SDT12S60, SiC Schottky	600 V, 12 A
Coupled Inductor	Magnetics Inc.	58867-A2 (μ=60) High-Flux Toroidal	500 μH @ FL, 700-750 μH @ NL, N1 = 73, N2 = 15
HF Transformer	Magnetics Inc.	P-49925-UC, Ferrite Core	Np = 34, Ns = 80
HF inverter Controller IC	Texas Instruments	UC3875	Phase shift controller
Heat Sink	Aavid Thermalloy	60095	1.90 °C/W, W= 4.12” H=1.75”, Area= 36.8 in^2

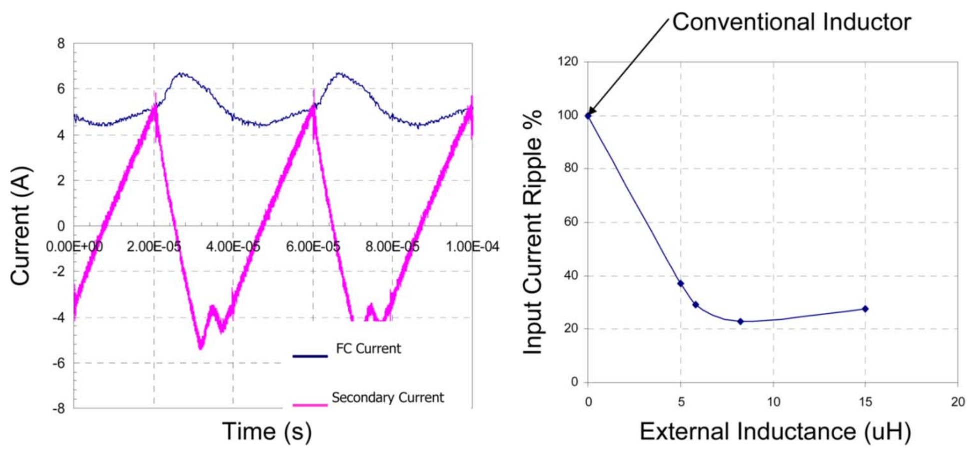

Fig. 9. Coupled inductor performance results: (a) input current splits between the dc and the ac windings for an optimum value of external inductance; and (b) experimentally-observed input ripple-current variation (relative to the ripple current obtained without using the coupled-inductor) in the dc winding with (manual) variations in the external inductance. (FL: full load; NL: no load).

III. RESULTS AND DISCUSSION

To validate the performance of the PCS, we developed a working prototype [shown in Fig. 8(a)] for the following specifications: (a) nominal planar SOFC stack voltage: 70 V, (b) output voltage: ~110 V RMS, single phase, 60 Hz (c) output power: 5 kW (d) switching frequency of dc–dc converter: 20 kHz (e) switching frequency of dc–ac converter: 20 kHz. Table I is a list for key power stage components. The results presented in this section demonstrate the operation and the notable features of the individual subsystems of the proposed PCS topology. Fig. 8(b) shows an experimental setup which was used to obtain characterization data using scaled testing on a planar SOFC stack [as shown in Fig. 8(b) and (c)]. Full-scale testing was done using fuel-cell emulator from California Instruments (model number XDS 80–62).

A. Performance of the ZRBC

In our experimental prototype a small external tunable inductor was used in series with the secondary winding of the coupled-inductor to obtain a finer control over the HF current ripple.

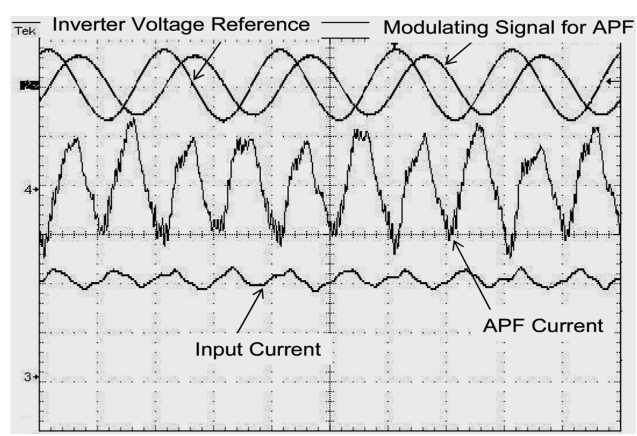

Fig. 10. Input current ripple reduction with APF (Ch3: 20 A/div, 10 ms/div and Ch4: 20 A/div, 10 ms/div).

Fig. 9(b) shows the percentage of ripple reduction achieved by the coupled inductor as the external inductance is tuned. For an external inductance of 7.6 μH, the fuel cell HF current ripple is reduced to 20% of the maximum possible HF ripple. The rest 80% of the HF current ripple is supplied by the secondary

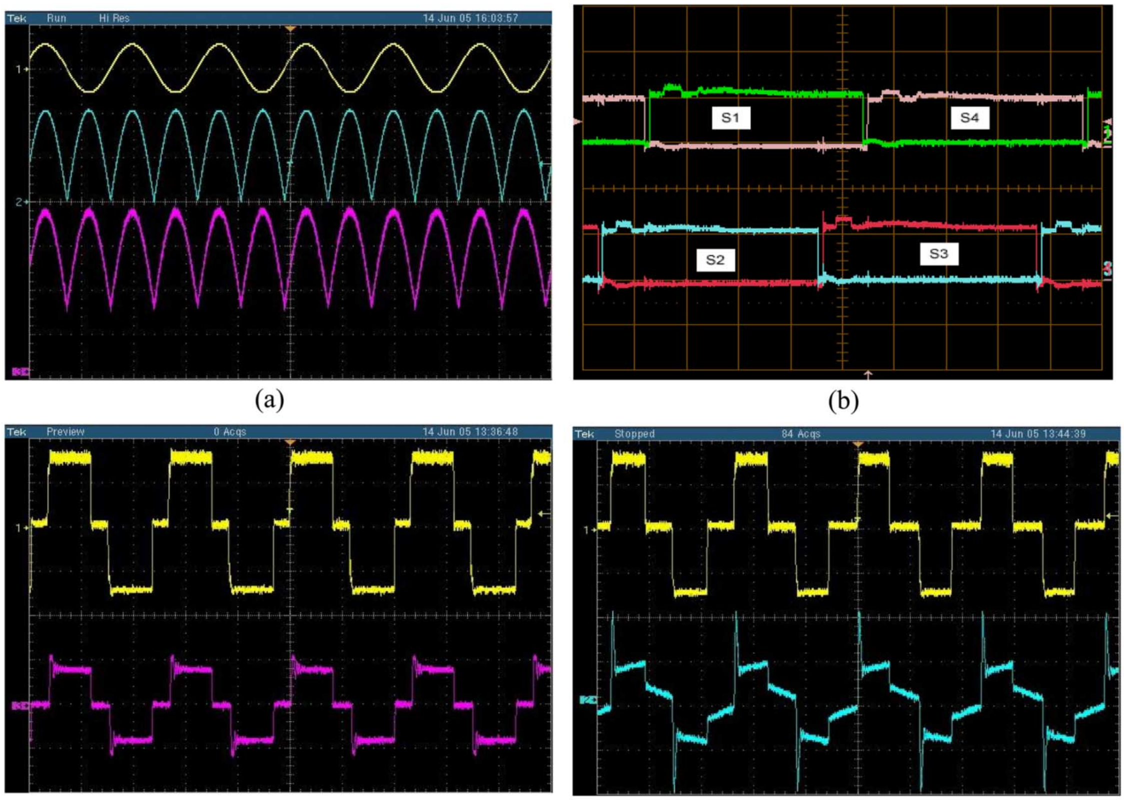

(a) (b)

(c) (d)

Fig. 11. Demonstration of the HF inverter operation. (a) Control signal (top, 500 mV/div 10 ms/div), rectified control signal (center, 1 V/div 10 ms/div), rectified control signal with 1.3 V (which is input to the UC3875) (bottom, 1 V/div 10 ms/div). (b) Gating pulse for HF inverter switches (10 V/div). (c) HF transformer primary voltage (top, 200 V/div) and HF transformer secondary voltage (bottom, 500 V/div). (d) HF transformer primary voltage (top, 200 V/div) and current waveforms (50 A/div).

winding of the coupled inductor as shown in Fig. 9(a). Fig. 10 demonstrates the low-frequency current injection by the APF. It can be seen that the PCS low-frequency peak input current is reduced to 15% of the maximum possible input current ripple. The remaining 85% of the current ripple flows through the secondary winding of coupled inductor. Such a reduction in fuel cell current ripple will significantly improve the stack efficiency as well as fuel utilization and will potentially enhance the life of the fuel-cell stack. The efficiency of the ZRBC is shown in Fig. 15. This efficiency figure is obtained with 4 ZRBCs in parallel (to share the large source current at higher output power), as mentioned in Section II. Fig. 15 shows that the efficiency of the ZRBC stage drops at lower power. This is because the ZRBC switches are hard-switched and hence at lower power, when the switching losses become dominant (as compared to conduction loss), the efficiency of the converter reduces.

B. Performance of the DC–AC Converter

For the HF inverter, the PSZVS SPWM is implemented using the UC3875 phase-shift controller. The control signals, the gating pulses for all 4 switches, the transformer primary current and voltage waveforms, and transformer secondary voltage are shown in Fig. 11. Fig. 11(d) shows a spike in the primary current, which is due to the reverse recovery of the LFSC diode (reflected on to the primary side) when the secondary voltage changes polarity. This can be alleviated using a faster diode and a snubber. The primary-side voltage shown in Fig. 11(c) indicates that the maximum voltage stress on the power MOSFETs of the HF inverter is around 175 V, which is well within the device limit.

Fig. 12(a) shows that as leakage of the HF transformer increases, the ZVS range of the HF inverter, for a given RMS load current and with cyclic variation of the output current, increases. However, the transformer efficiency reduces due to loss of duty cycle [that can be calculated using (13)] as shown in Fig. 12(b) in per unit (PU). Additionally, as explained in Section II, higher leakage will lead to higher duty ratio due to enhanced commutation delay and consequently, higher conduction loss in the switches of the HF inverter. It turns out that for 20 kHz switching frequency, the conduction loss is more dominating as the load power increases. Therefore, from a thermal-management standpoint, it is preferred to choose a transformer with lower leakage inductance to reduce conduction loss at higher power. However, this will reduce the effectiveness of the ZVS at lower power, where the switching losses are more dominating. Therefore, a careful selection of the transformer leakage inductance is necessary. Fig. 12(a) shows that for values of leakage inductance around 0.5–1 μH, a good compromise between conduction and switching losses is obtained. HF transformer designs using different winding arrangements were made, as shown in Fig. 13(a) and (b) with respective leakage inductances of 1.2 μH and 450 nH. We selected the second design. For this design, primary and secondary windings are distributed over the entire length of the

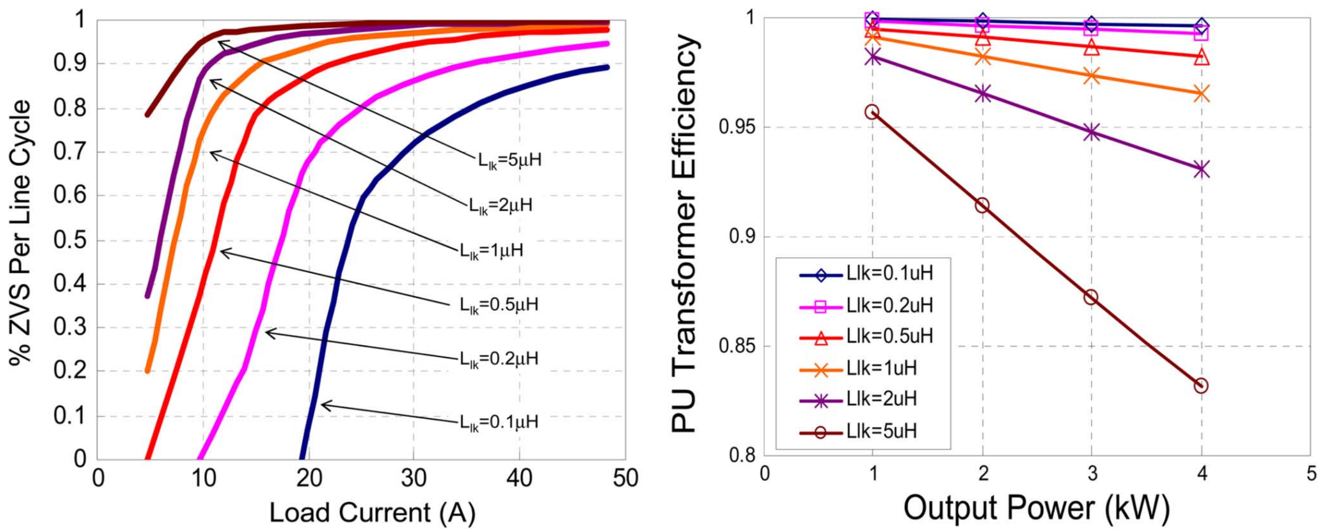

(a) (b)

Fig. 12. (a) Parametric plot showing the percentage ZVS achievable versus load current for different values of leakage inductances. (b) Transformer efficiency versus output power for various values of leakage inductances.

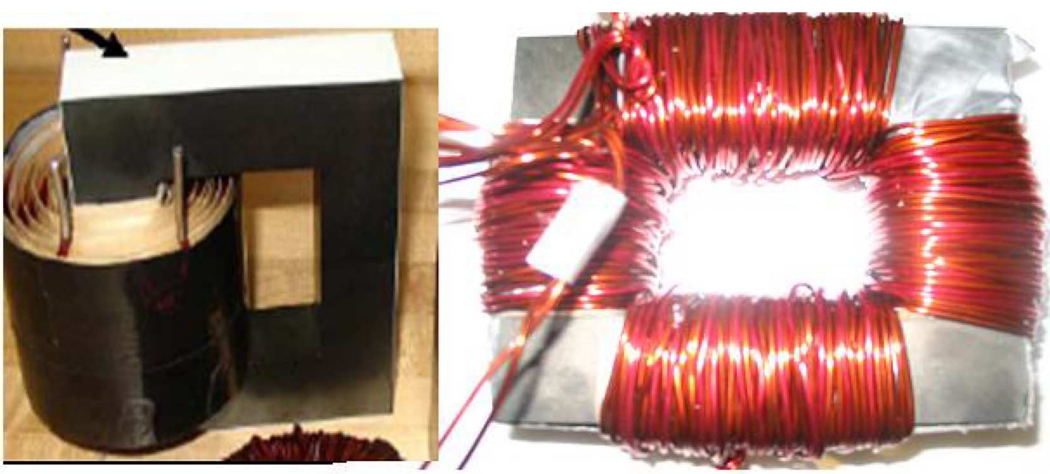

Fig. 13. Two different winding arrangements for a 5 kW, 20 kHz isolation transformer fabricated using P-49925-UC, ferrite core. (a) Primary and secondary windings on the same leg using an AWG 10 solid copper wire. The leakage inductance was measure to be 1.2 μH. (b) Primary and secondary windings distributed over the entire length of the core using a double-stranded AWG 14 copper wire. The leakage inductance was measured to be 450 nH.

core using a 2 strand (bifilar) AWG 14 copper wire. From a skin-effect point of view, a higher gauge can be used; however, it also leads to higher conduction loss, which is more dominating for the 20 kHz design at higher load power.

Fig. 14 shows the operation of the LFSC near unity power-factor. It can be seen in Fig. 14(c) that when the polarities of the output voltage and the current are the same, the LFSC switches at line frequency. Otherwise, the LFSC switches at 20 kHz. Because high-frequency switching is negligible, such a mechanism results in a significant reduction in the switching losses of the LFSC, as shown in Fig. 14(c). Fig. 14(d) shows that the LFSC is properly rectifying the output voltage of the HF inverter.

Fig. 15(a) shows the experimentally obtained efficiencies of the overall PCS, ZRBC, and the dc–ac converter. The obtained overall efficiency at full load is approximately 92% and the peak efficiency of 92.4% is obtained at 3 kW of output power. Fig. 15(b) is the predicted combined efficiency of the planar SOFC and the PCS. The obtained efficiency numbers in Fig. 15(b) are the products of measured PCS overall efficiency and modeled fuel-cell stack efficiency values for different values of current ripple (varying from 5% to 97%). Fig. 16 shows the output voltage and output current of the PCS near full-load condition. It also shows the satisfactory response of the PCS for both steady-state and dynamic conditions.

IV. Conclusion

This paper presents a ZRF based low-cost fuel-cell PCS, which can meet a cost target of $40/kW in volume production. The PCS comprises a ZRF based boost converter (that is described as ZRBC), which is followed by an isolated dc–ac converter comprising a HF inverter (which reduces device voltage stress) and a line frequency switched cycloconverter (LFSC). Apart from fuel cell, the PCS can be potentially used for applications (of comparable and even power) encompassing energy sources including RFCs, photovoltaic arrays, and bat-

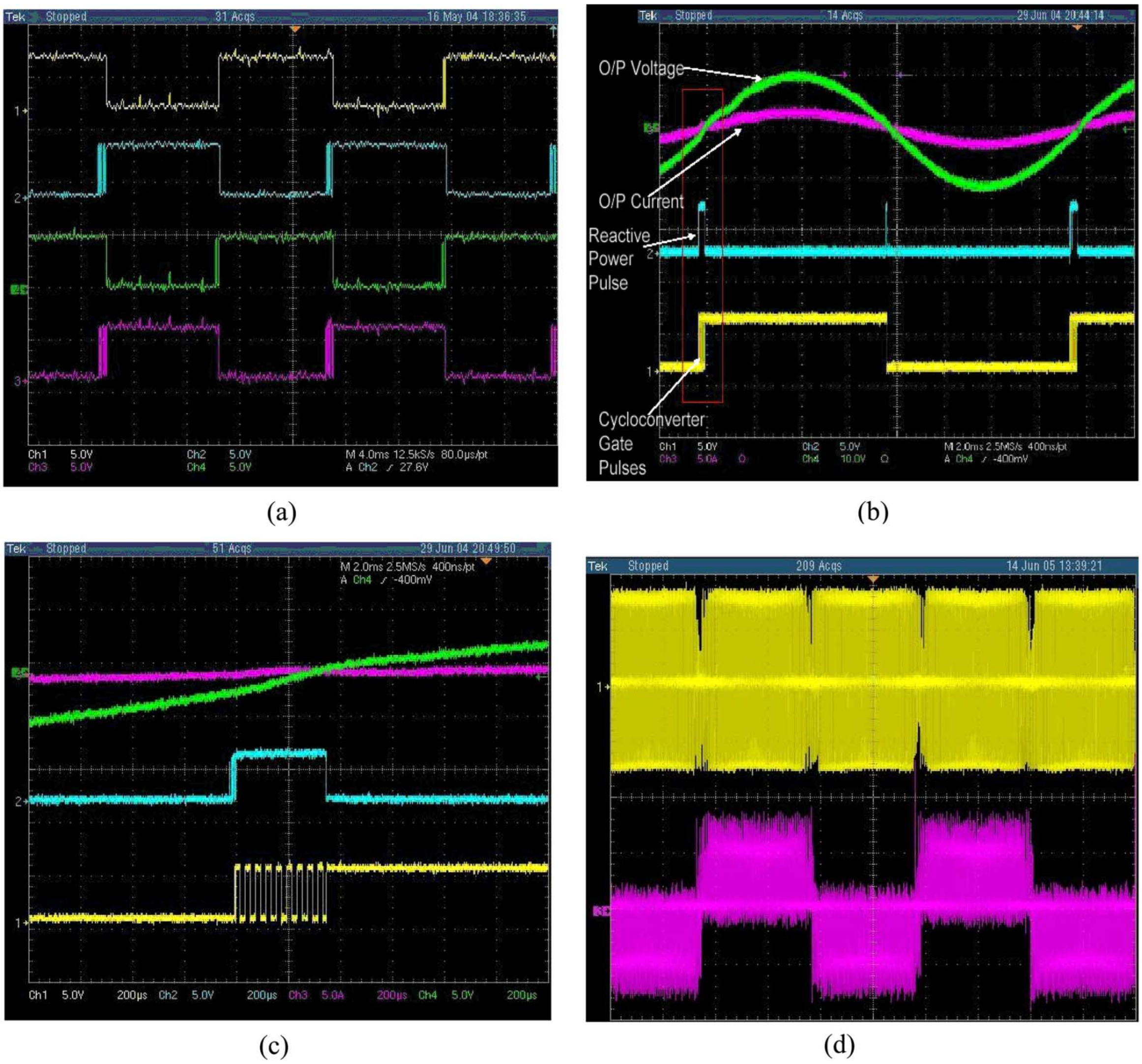

Fig. 14. Demonstration of the LFSC operation: (a) gating pulses (10 V/div) for Q1-Q4; (b) filtered output voltage and current (top), reactive power information (center), gating pulse for Q1 (bottom); (c) an expanded view of the rectangular portion of plot (b); and (d) output voltage (bottom, 500 V/div 10 ms/div) before the filter for a given HF transformer primary voltage (top, 200 V/div 10 ms/div).

teries. The PCS can also be extended to 240 V applications by dynamically changing the transformer turns ratio before power-conversion is initiated.

The PCS has two key features: i) a ZRF and ii) an isolated dc–ac converter comprising a zero-voltage-switching (ZVS) multilevel HF inverter followed LFSC. The ZRF comprises a coupled-inductor based passive solution for mitigating stack high-frequency ripple current and an active power filter (APF) for mitigating the stack low-frequency ripple current, thereby yielding several advantages as follows.

- Stack operates close to its maximum efficiency point, thereby increasing the overall efficiency of the energy system comprising the stack and the PCS;
- Ripple mitigation precludes stack underutilization (and reduces system cost), which would be otherwise necessary to accommodate the additional ripple current;
- Enhances the performance of the stack and potentially minimizes its long-term degradation.

However, reduction of the ripple current to very close to zero will requires optimal tuning of the coupled inductor and the APF parameters. Further, the ZRF increases the order of the ZRBC (as compared to a conventional boost converter), which has to be addressed by the control scheme.

The efficiency of the PCS is high on account of three reasons.

- Four ZRBC modules are connected in parallel to reduce the conduction losses, which could be otherwise high due to the low-voltage and high-current stack;
- HF inverter operates with ZVS, which reduces the switching loss of the power devices;
- Controlled switches of the LFSC operates at line frequency (under unity power factor), which practically eliminates their switching losses;
- The transformer leakage inductance has been so chosen such that a good compromise is obtained between effectives of the ZVS and increased commutation losses.

However, because the switches of the ZRBC are hard-switched, its switching losses become progressively more dominating at lower power when the efficacy of using paralleled module to reduce conduction losses reduces. Use of power MOSFETs with faster switching response (and comparable on-state resistances) may help; soft switching may be another option. For the dc–ac converter, for a finite leakage inductance

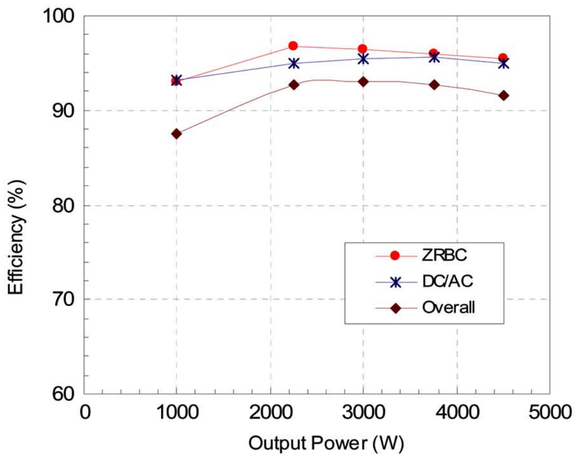

(a)

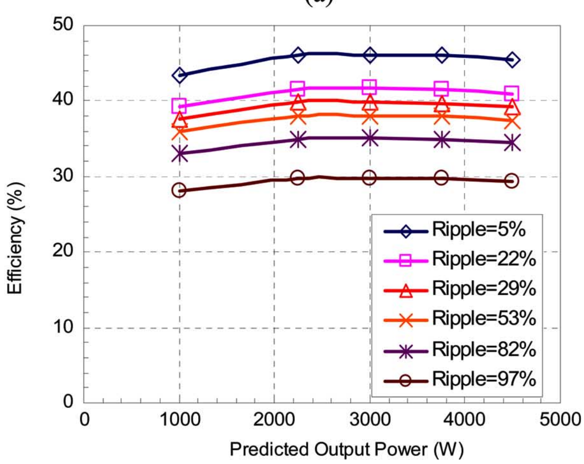

(b)

Fig. 15. (a) Measured efficiency for the proposed PCS and its subsystem including parasitic losses. (b) Combined efficiency of the planar SOFC stack and PCS for various fuel-cell ripple current.

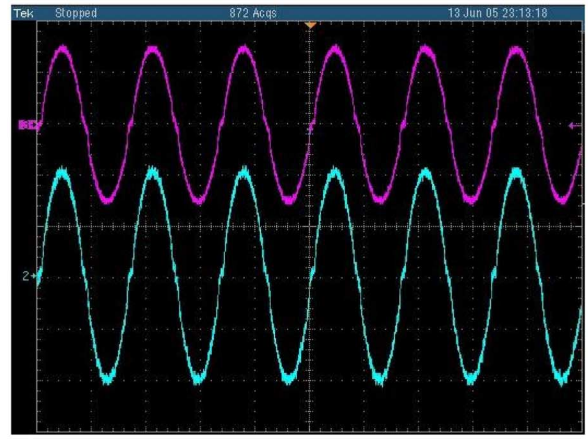

(a)

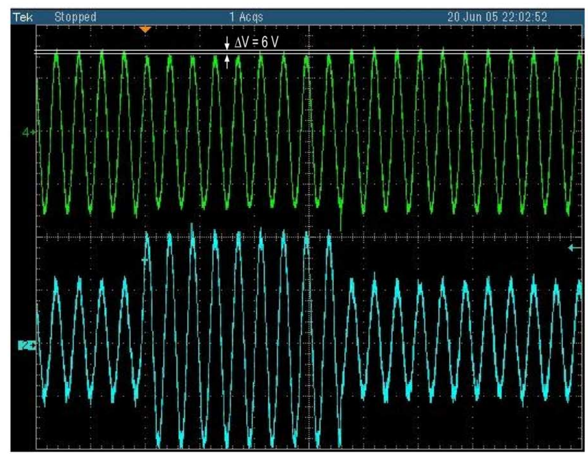

(b)

Fig. 16. (a) Steady-state output voltage (top trace at 100 V/div and 10 ms/div) and output current (bottom trace at 25 A/div and 10 ms/div) of the inverter near full load. (b) Output voltage (top trace at 100 V/div and 40 ms/div) and output current (bottom trace at 25 A/div and 40 ms/div) of the inverter when the load changes from 2200 W to 4500 W and back to 2200 W.

of the HF transformer, there is a tradeoff between the effectiveness of ZVS of the HF inverter and the commutation loss of both the ac–ac LFSC and the HF inverter. So, transformer design needs to be carefully carried out. Additionally, usage of low on-stage drop IGBTs for the LFSC will help. An additional loss is due to the reverse recovery of the LFSC diodes. This can be alleviated by using diodes with faster recovery time and snubbers if necessary. Finally, though the controlled switches of the LFSC theoretically operate at line-frequency under unity power factor, the switches do forced commutation when the power factor is not unity. For near-unity-power-factor operation, this loss is negligible though.

Appendix A
Extension to Other Applications

A. Regenerative Fuel-Cell (RFC) Application

An RFC can operate as an electrolyzer and in this mode it absorbs electricity (e.g., from grid or photovoltaic source) to generate hydrogen and oxygen that can be used later to generate electricity using the RFC in fuel cell mode. Lighter than a separate electrolyzer and generator, a RFC is an excellent energy

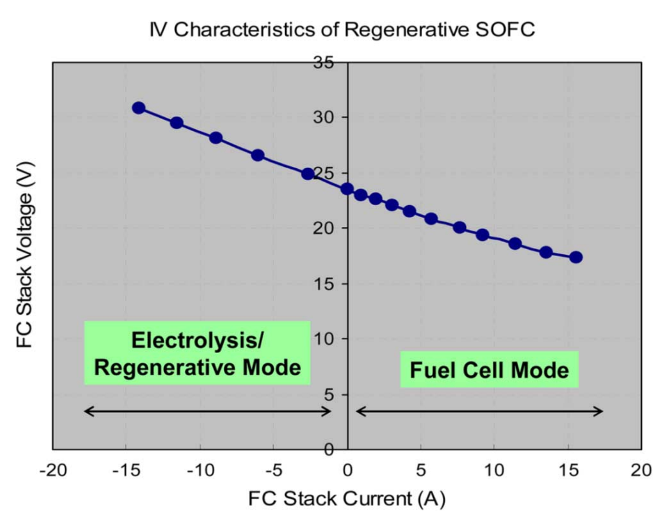

Fig. 17. Experimental polarization curve for a 20-cell regenerative SOFC.

source in applications where weight is a concern [22]. Fig. 17 is the polarization curve for a 20-cell regenerative SOFC stack. The negative current indicates the power flow into the RFC. The proposed PCS can operate in a rectifier mode by replacing the

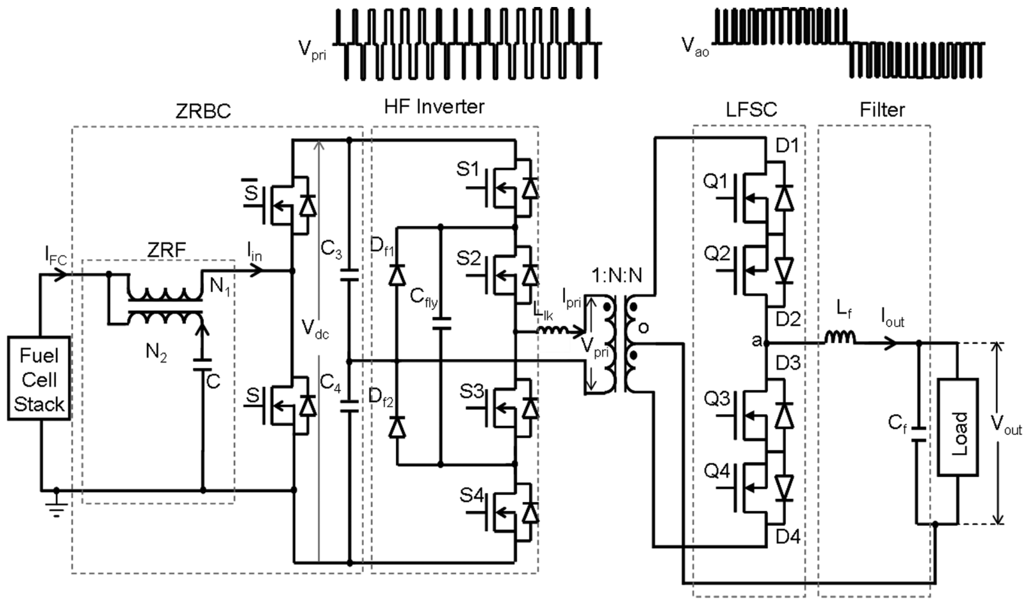

Fig. 18. Modified PCS schematic for bidirectional power flow.

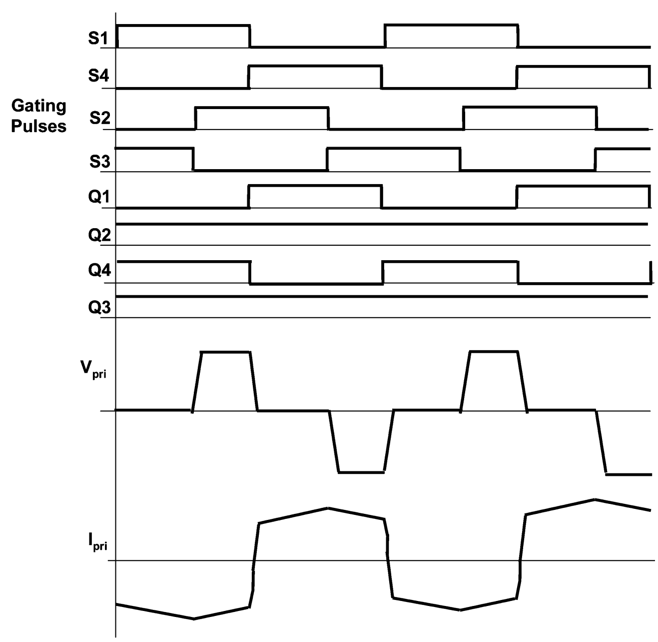

Fig. 19. Schematic waveforms of the proposed PCS for rectifier mode of operation when feeding power to a RFC. Forced commutation of the cycloconverter (unlike LFSC) is necessary because the polarities of the source current (which is opposite to that of I_{out}) and source voltage are opposite.

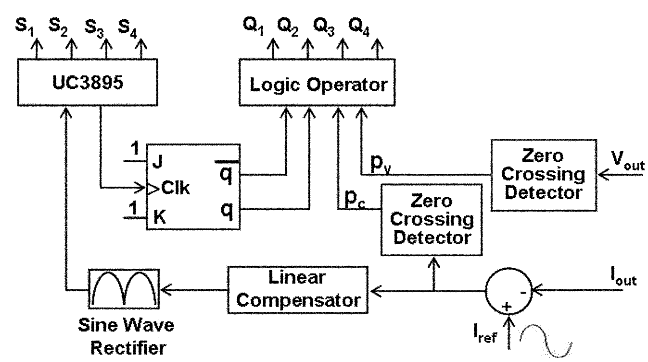

Fig. 20. Overall control scheme for the rectifier mode of operation.

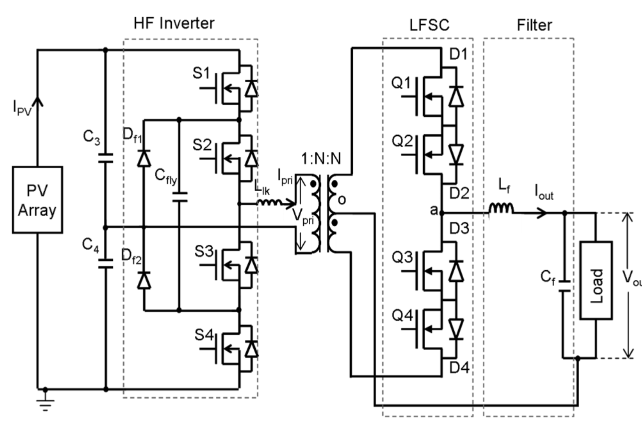

Fig. 21. Modified PCS schematic for PV application.

ZRBC diode D by a MOSFET $(\bar{S})$ as shown in Fig. 18. The schematic waveforms and the controller structure for the rectifier mode operation are shown in Figs. 19 and 20. For the rectifier mode of operation, input ac-current mode controller (as shown in Fig. 20) is implemented to inject current at near unity power factor.

B. High-Voltage Photovoltaic Application

The proposed PCS can be extended to photovoltaic (PV) applications [32] (where the output voltage of the array is high) by eliminating the front end ZRBC as shown in Fig. 21. For such an application, the controller shown in Fig. 2(c) can be used without any changes.

ACKNOWLEDGMENT

S. K. Maxumder acknowledges the help of Ph.D. student T. Sarkar for his help with preparing the revised manuscript. Finally, the authors acknowledge the useful feedback of one of the reviewers.

Work presented in this paper is protected by Patent Application 20050141248: S. K. Mazumder, R. K. Burra, and K. Acharya, *A novel efficient and reliable dc–ac converter for fuel cell power conditioning*, University of Illinois, USPTO.

References

[1] C. Haynes and W. J. Wepfer, "Characterizing heat transfer within a commercial-grade tubular solid oxide fuel cell for enhanced thermal management," *Int. J. Hydrogen Energy*, vol. 26, pp. 369–379.

[2] [Online]. Available: www.nfcrc.uci.edu/UFFC/PowerElectronics /PDFs/24_%20Gemmen.pdf

[3] S. H. Pyke, A. J. Burnett, and R. T. Leah, "Systems development for planar SOFC based power plant," ETSU F/01/00195/REP, DTI/Pub UNR 02/868, Contractor: ALSTOM Research and Technology Centre.

[4] J. Lai and C. Liu, "Low frequency current ripple reduction technique with active control in a fuel cell power system with inverter load," in *Proc. IEEE Power Electronics Specialists Conf.*, Jul. 2005, pp. 2905–2911.

[5] H. Xu, E. Qiao, X. Guo, X. Wen, and L. Kong, "Analysis and design of high power interleaved boost converters for fuel cell distributed generation system," in *IEEE Power Electronics Specialists Conf.*, Jul. 2005, pp. 140–145.

[6] W. Choi, P. N. Enjeti, and J. W. Howze, "Development of an equivalent circuit model of a fuel cell to evaluate the effects of inverter ripple current," in *Proc. IEEE Applied Power Electronics Conf. and Expo.*, 2004, pp. 355–361.

[7] Y. R. Novaes and I. Barbi, "Low frequency ripple current elimination in fuel cell systems," Fuel Cell Seminar 2003 [Online]. Available: http:// www.energychallenge.org/FuelCellSeminar.pdf

[8] G. K. Andersen, C. Klumpner, S. B. Kjaer, and F. Blaabjerg, "A new green power inverter for fuel cells," in *Proc. IEEE Power Electronics Specialists Conf.*, 2002, pp. 727–733.

[9] R. Gopinath, S. S. Kim, and P. Enjeti, "Development of a low cost fuel cell inverter with DSP control," in *Proc. IEEE Power Electronics Specialists Conf.*, 2002, pp. 1256–1262.

[10] G. W. Pradeep, H. Mohammad, and P. Famouri, "High efficiency low cost inverter system for fuel cell application," Fuel Cell Seminar 2003 [Online]. Available: http://www.energychallenge.org/FuelCellSeminar.pdf

[11] J. Mazumdar, I. Batarseh, and N. Kutkut, "High frequency low cost dc-ac inverter design with fuel cell source for home applications," in *Proc. IEEE Industry Applications Conf.*, 2002, pp. 789–794.

[12] A. M. Tuckey and J. N. Krase, "A low-cost inverter for domestic fuel cell applications," in *Proc. IEEE Power Electronics Specialists Conf.*, 2002, pp. 339–346.

[13] P. T. Krein and R. Balog, "Low cost inverter suitable for medium-power fuel cell sources," in *IEEE Power Electronics Specialists Conf.*, 2002, pp. 321–326.

[14] H. Ertl, J. W. Kolar, and F. C. Zach, "A novel multicell DC-AC converter for applications in renewable energy systems," *IEEE Trans. Ind. Elect.*, pp. 1048–1057, 2002.

[15] J. Wang and F. Z. Peng, "A new low cost inverter system for 5 kW fuel cell," Fuel Cell Seminar 2003 [Online]. Available: http://www.energychallenge.org/FuelCellSeminar.pdf

[16] T. P. Bohn and R. D. Lorenz, "A low-cost inverter for domestic fuel cell applications," Fuel Cell Seminar 2003 [Online]. Available: http:// www.energychallenge.org/FuelCellSeminar.pdf

[17] T. Kawabata, H. Komji, and K. Sashida, "High frequency link dc/ac converter with PWM cycloconverter," in *IEEE Industrial Application Society Conf.*, 1990, pp. 1119–1124.

[18] S. Deng and H. Mao, "A new control scheme for high-frequency link inverter design," in *IEEE Applied Power Electronics Conf. Expo.*, 2003, pp. 512–517.

[19] R. K. Burra, S. K. Mazumder, and R. Huang, "A low-cost fuel-cell (FC) power electronic system (PCS) for residential loads," in *Proc. IEEE Int. Telecommunications Energy Conf.*, 2004, pp. 468–478.

[20] S. K. Mazumder, "Fuel cell power conditioner for stationary power system: Towards optimal design from reliability, efficiency, and cost standpoint, Keynote Lecture," presented at the Proc. ASME 3rd Int. Conf. on Fuel Cell Science, Engineering and Technology, Yipsilanti, MI, May 23–25, 2005, FUELCELL2005-74178.

[21] F. Canales, P. Barbosa, and F. C. Lee, "A zero-voltage and zero-current switching three-level DC/DC converter," *IEEE Trans. Power Elect.*, vol. 17, no. 6, pp. 898–904, 2002.

[22] [Online]. Available: www.llnl.gov/str/Mitlit.html

[23] J. Wang, F. Z. Peng, J. Anderson, A. Joseph, and R. Buffenbarger, "Low cost fuel cell inverter system for residential power generation," in *Proc. IEEE Applied Power Electronics Conf. Expo.*, 2004, pp. 367–373.

[24] W. Rong-Jong and D. Rou-Yong, "High efficiency power conversion for low power fuel cell generation system," *IEEE Trans. Power Elect.*, vol. 20, no. 4, pp. 847–856, 2005.

[25] S. Pradhan, S. K. Mazumder, J. Hartvigsen, and M. Hollist, "Effects of electrical feedbacks on planar solid-oxide fuel cell," *ASME J. Fuel Cell Sci. Tech.*, vol. 4, pp. 154–166, May 2007.

[26] J. R. Pinhiero and I. Barbi, "The three-level ZVS-PWM DC-to-DC converter," *IEEE Trans. Power Elect.*, vol. 8, pp. 486–492, 1993.

[27] G. Bloom and R. Sevens*, Modern DC-to-DC Switchmode Power Converter Circuits*. New York: Van Nostrand-Reinhold, 1985.

[28] [Online]. Available: http://www.netl.doe.gov/seca/industry.html

[29] S. C. Singhal and K. Kendall*, High-Temperature Solid Oxide Fuel Cells: Fundamentals, Design and Applications*. Burlington, MA: Elsevier Science., 2003.

[30] *Fuel-Cell Handbook*, 7th ed. Morgantown, West Virginia: EG&G Technical Services Inc., Department of Energy (DOE), 2004.

[31] R. Gemmen, "Analysis for the effect of inverter ripple current on fuel cell operating condition," *J. Fluids Eng.*, vol. 125, no. 3, pp. 576–585, 2003.

Sudip K. Mazumder (SM'02) is the Director of the Laboratory for Energy and Switching-electronics Systems (LESES) and an Associate Professor in the Department of Electrical and Computer Engineering at the University of Illinois, Chicago. He has over 10 years of professional experience and has held R&D and design positions in leading industrial organizations. His current areas of interests are interactive power-electronics/power networks, renewable and alternate energy systems, and new device and systems-on-chip enabled higher power density.

Dr. Mazumder received the 2006 Diamond Award from the University of Illinois, Chicago for Outstanding Research Performance. He also received the Office of Naval Research (ONR) Young Investigator Award, National Science Foundation (NSF) CAREER Award, and the Department of Energy's (DOE) Solid State Energy Conversion Alliance (SECA) Award in 2005, 2003, and 2002, respectively and a Paper Prize Award from the IEEE TRANSACTIONS ON POWER ELECTRONICS and the IEEE Power Electronics Society (PELS) in 2002. He has been the Editor-in-Chief of the *International Journal of Power Management Electronics* since 2007. He is also an Associate Editor for the IEEE TRANSACTIONS ON INDUSTRIAL ELECTRONICS and was the Associate Editor for IEEE POWER ELECTRONICS LETTERS until 2005. He has published over 60 refereed and invited journal and conference papers and is a reviewer for six international journals.

Rajni K. Burra (M'06) received the B.Tech. degree in electronics and communication engineering from the Indian Institute of Technology (IIT), Kharagpur in 2000, the M.S. and the Ph.D. degrees, both in electrical engineering from the University of Illinois, Chicago in the years 2003 and 2006, respectively. He is currently working as a Research Engineer at the General Electric Corporate Research Center, Bangalore, India.

Dr. Burra's research interests include nonconventional and renewable energy systems, active power filtering, and power semiconductor devices. He has published over 13 refereed international journal and conference papers.

Kaustuva Acharya (S'06) received the Bachelor of Engineering degree in electronics and communication engineering from the Regional Engineering College (now, the National Institute of Technology), Bhopal, India, in 2000, and the M. Sci. degree in electrical engineering from the University of Illinois, Chicago, in 2003, where he is currently pursuing the Ph.D. degree in electrical engineering.

He is a Research Assistant at the Laboratory for Energy and Switching-electronics Systems, University of Illinois at Chicago. His research interests include power electronics for renewable and alternate energy sources, and modeling, analyses, and control of interactive power networks for distributed power systems. He has published over 15 refereed international journal and conference papers.

Mr. Acharya is a reviewer for the IEEE TRANSACTIONS ON POWER ELECTRONICS, IEEE TRANSACTIONS ON INDUSTRIAL ELECTRONICS and several international conferences.